Secondary flow in turbulent ducts with increasing aspect ratio

R. Vinuesa,[1,*] P. Schlatter,[1] and H. M. Nagib[2]
[1]*Linné FLOW Centre, KTH Mechanics and Swedish e-Science Research Centre (SeRC), Stockholm SE-100 44, Sweden*
[2]*MMAE Department, Illinois Institute of Technology, Chicago, Illinois IL 60616, USA*

(Received 15 December 2017; published 17 May 2018)

Direct numerical simulations of turbulent duct flows with aspect ratios 1, 3, 5, 7, 10, and 14.4 at a center-plane friction Reynolds number $\mathrm{Re}_{\tau,c} \simeq 180$, and aspect ratios 1 and 3 at $\mathrm{Re}_{\tau,c} \simeq 360$, were carried out with the spectral-element code NEK5000. The aim of these simulations is to gain insight into the kinematics and dynamics of Prandtl's secondary flow of the second kind and its impact on the flow physics of wall-bounded turbulence. The secondary flow is characterized in terms of the cross-plane component of the mean kinetic energy, and its variation in the spanwise direction of the flow. Our results show that averaging times of around 3000 convective time units (based on duct half-height h) are required to reach a converged state of the secondary flow, which extends up to a spanwise distance of around $\simeq 5h$ measured from the side walls. We also show that if the duct is not wide enough to accommodate the whole extent of the secondary flow, then its structure is modified as reflected through a different spanwise distribution of energy. Another confirmation of the extent of the secondary flow is the decay rate of kinetic energy of any remnant secondary motions for $z_c/h > 5$ (where z_c is the spanwise distance from the corner) in aspect ratios 7, 10, and 14.4, which exhibits a decreasing level of energy with increasing averaging time t_a, and in its rapid rate of decay given by $\sim t_a^{-1}$. This is the same rate of decay observed in a spanwise-periodic channel simulation, which suggests that at the core, the kinetic energy of the secondary flow integrated over the cross-sectional area, $\langle K \rangle_{yz}$, behaves as a random variable with zero mean, with rate of decay consistent with central limit theorem. Long-time averages of statistics in a region of rectangular ducts extending about the width of a well-designed channel simulation (i.e., extending about $\simeq 3h$ on each side of the center plane) indicate that ducts or experimental facilities with aspect ratios larger than 10 may, if properly designed, exhibit good agreement with results obtained from spanwise-periodic channel computations.

DOI: 10.1103/PhysRevFluids.3.054606

I. INTRODUCTION

Turbulent duct flows of different aspect ratios AR (defined as the duct width W_d divided by its total height H) are of great importance for a number of technological applications due to the complicated interactions of wall-bounded turbulence with the corner. Such applications include complex flow in turbomachinery, heat exchangers, diffusers, ducts used in refrigeration, etc., and the development of the secondary flow at the corner is a fundamental mechanism present in several other applications such as in the junction between an airplane wing and the fuselage or in open channels and rivers. Moreover, the flow through a fully developed turbulent duct is an interesting case from a scientific point of view, since it allows us to study the features of wall-bounded turbulence with mean

*rvinuesa@mech.kth.se

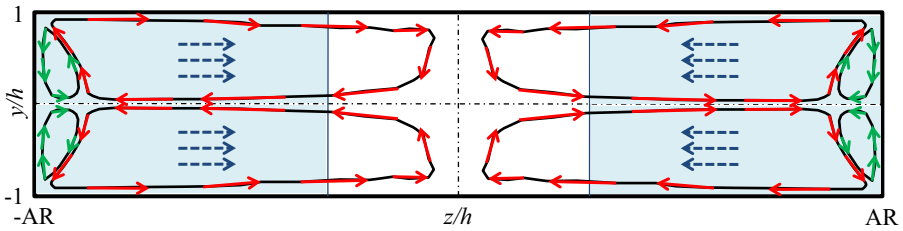

FIG. 1. Schematic view of the three-dimensional effects present in fully developed turbulent duct flows. The blue regions represent the side-wall boundary layers and the dashed blue arrows show that they accelerate the flow in the duct center plane. Red and green arrows indicate the flow direction in the secondary vortices on the horizontal and vertical walls, respectively.

three-dimensional effects. Such effects include, on the one hand, the growth of boundary layers on the side walls, which—as shown schematically in Fig. 1—reach a certain thickness in the spanwise direction depending on the duct aspect ratio and Reynolds number. The side-wall boundary layers produce an acceleration of the flow core at the duct center plane, thus increasing the local skin friction. Another three-dimensional effect is the presence of four secondary vortices located on the horizontal walls, and four more on the vertical ones. The vortices on the horizontal walls convect near-wall fluid at the duct center plane toward the outer region, and then recirculate the flow towards the side wall, as illustrated in Fig. 1. This results in a local decrease of the center plane wall-shear stress, the value of which depends on the respective contributions of side-wall boundary layers and secondary flow in terms of AR and Re, as discussed by Vinuesa *et al.* [1]. Finally, the secondary vortices on the vertical walls convect fluid toward the corners through the line tangent to the vortices on the horizontal walls. The secondary flow present in straight, fully developed turbulent ducts was denoted by Prandtl [2] as "secondary flow of second kind." This type of secondary flow, which lies in the y-z plane (where y and z are the vertical and spanwise directions respectively), normal to the streamwise direction x, arises from the Reynolds-stress difference $\overline{v^2} - \overline{w^2}$ and the Reynolds-stress component $\overline{vw}$. Because of the Reynolds-stress-induced nature of this kind of secondary flow, currently available Reynolds-averaged Navier-Stokes (RANS) models widely used in industry in general fail to predict its effect on the flow. As pointed out by Spalart [3], only RANS models with constitutive relations between the Reynolds stresses and the mean flow which do not assume that both tensors are aligned (as in the traditional Boussinesq approximation) can predict the presence of this kind of secondary flow. It is important to note that the secondary flow of second kind is a mean flow feature, and even though it only amounts to around 2–3% of the bulk velocity U_b [4] and, as already observed experimentally in the 1960s and 1970s by Hoagland [5], Gessner and Jones [6], and Gessner [7], its impact on the flow may be very relevant.

A flow case that has received some attention from the computational point of view is the turbulent flow through a square duct, with the first direct numerical simulations (DNSs) carried out in the early 1990s by Gavrilakis [8] and Huser and Biringen [4]. The DNS by Gavrilakis [8] was carried out at a friction Reynolds number $\mathrm{Re}_\tau = 150$ (where Re_τ is defined in terms of the duct half-height h and the average friction velocity $\overline{u}_\tau = \sqrt{\overline{\tau}_w/\rho}$, where $\overline{\tau}_w$ is the mean wall-shear stress averaged over the four walls, which is related to the streamwise pressure drop, and ρ is the fluid density). One of the most interesting outcomes of the work by Gavrilakis [8] is the observation that, although the streamlines obtained from the mean stream function Ψ in the y-z plane show the two counter-rotating vortices at the corner, the mean streamwise vorticity field Ω_x exhibits two vorticity cells of opposite signs within each of those vortices. The study by Huser and Biringen [4], at a higher $\mathrm{Re}_\tau = 300$, shed some light on the mechanisms responsible for the formation of the secondary flow: By analyzing the spanwise evolution of the Reynolds-stress tensor shear components, they found that the secondary flow is produced by the interactions of bursting events from the horizontal and vertical walls close to the corner, which basically lead to a redistribution of $\overline{v^2}$ fluctuations to the $\overline{w^2}$ component, responsible for

the creation of the secondary vortices. The more recent DNS by Pinelli *et al.* [9] at Re_τ values up to 300 showed that, as opposed to spanwise-periodic channels, the corner determines the location of the first near-wall streak and its type: A high-speed streak is found at an inner-scaled spanwise distance $z_c^+ \simeq 50$ (where we define the variable z_c with its origin at the corner), followed by a low-speed streak, separated a spanwise length of approximately $\lambda_z^+/2 \simeq 50$ (note that the spanwise distance between two streaks of the same type is $\lambda_z^+ \simeq 100$ [10,11]). In the present study, the superscript "+" denotes inner scaling based on the friction velocity u_τ (it will be specified whether it is evaluated at the center plane or averaged over the four walls) and the viscous length $\ell^* = \nu/u_\tau$ (where ν is the fluid kinematic viscosity). Note that the value of z_c^+ depends on the corner geometry, as recently shown by Marin *et al.* [12], who reported $z_c^+ \simeq 38$ in hexagonal ducts. The inner-scaled total width of the duct W_d^+ determines the number of streaks that can be sustained. The DNS work by Uhlmann *et al.* [13] at low Re with Re_τ up to around 175 was focused on the limiting state where the W_d^+ does not support the number of streaks required by the near-wall turbulence cycle, i.e., what they called the "marginally turbulent state." They observed this state at $\mathrm{Re}_\tau \simeq 77$, which has $W_d^+ \simeq 154$, a condition which can just sustain two high-speed streaks on the corners and a low-speed one at the center plane. This leads to a flow configuration in which short-term averages lead to a particular distribution of the secondary flow, with a total of four counter-rotating vortices located, alternatively, on the horizontal or vertical walls. Moreover, long-term averages reveal, also in the marginally turbulent state, the expected pattern with eight vortices. These numerical findings were supported by the experimental study carried out by Owolabi *et al.* [14], who also analyzed marginally turbulent flow effects. Another interesting DNS of the flow through a square duct was performed by Samanta *et al.* [15], who considered a configuration with three solid walls and a fourth wall composed of a porous bed. Their simulation was at $\mathrm{Re}_\tau^p \simeq 314$ (based on the average friction velocity over the porous bed $\overline{u}_\tau^p$), and their most interesting finding was the increase of secondary flow magnitude by a factor of four compared with a regular square duct with four solid walls, a consequence of the increased wall-normal transport across the porous bed.

Available numerical simulations of turbulent flow through square ducts in the literature include the DNS by Zhu *et al.* [16] at $\mathrm{Re}_\tau = 300$, the simulations by Raisei *et al.* [17] at Re_τ values up to 600, the work by Zhang *et al.* [18] also at Re_τ up to 600, and the recent DNS by Pirozzoli *et al.* [19] up to $\mathrm{Re}_\tau = 1000$. The simulation by Krasnov *et al.* [20] at a very high $\mathrm{Re}_{\tau,c} = 4253$ (where $\mathrm{Re}_{\tau,c}$ is defined in terms of the center-plane friction velocity $u_{\tau,c}$) was averaged for a very short averaging period, which might have lead to inaccurate results as mentioned in their own paper and also analyzed in terms of convergence by Vinuesa *et al.* [21]. Some other numerical studies of square ducts have used large-eddy simulation (LES), such as the work by Madabhushi and Vanka [22] at $\mathrm{Re}_\tau = 180$ and the study by Breuer and Rodi [23] at $\mathrm{Re}_\tau = 150$. Note that Breuer and Rodi [23] also performed an LES at a higher Reynolds number of 56 690 (based on hydraulic diameter and bulk velocity), more than 10 times higher than their low-Re case, but they found significant disagreement with experimental data. Another very high Reynolds number LES was performed by Yao *et al.* [24], up to an Re_τ value of 10 550, although their coarse mesh resolution (the number of grid points they used for their $\mathrm{Re}_\tau = 10\,550$ case is less than 1% of the total of grid points we consider in this study for a DNS at $\mathrm{Re}_\tau = 360$) suggests that there could be some inaccuracies in their results. The asymptotic conditions in turbulent duct flows were recently discussed by Spalart *et al.* [25]. Also note that in most cases these simulations were performed in short computational boxes, on the order of one fourth the length considered in the present work.

Despite the relative wealth of data of turbulent flow through square ducts, the flow through a rectangular duct has not received so much attention from a numerical point of view. This is in part due to the difficulties of using classic spectral methods (based on Fourier-Chebyshev discretizations) to simulate the flow through four walls, especially with a particular aspect ratio. The introduction of one additional parameter, AR, significantly increases the complexity of the problem due to the changes in secondary flow with the flow geometry. Some numerical studies of the flow through rectangular ducts include the AR = 3.33 duct flow at $\mathrm{Re}_\tau \simeq 300$ simulated by Ohlsson *et al.* [26] as part of their DNS of a three-dimensional diffuser and the LESs by Choi and Park [27] with

aspect ratios from 1 to 4 at $\mathrm{Re}_\tau = 150$. Recent DNSs of rectangular ducts at $\mathrm{Re}_{\tau,c} \simeq 180$ and 330, with AR values from 1 to 10, have been reported by Vinuesa *et al.* [1,28] with emphasis on the characterization of the wall-shear stress dependence with aspect ratio. The focus of the present study is the characterization of the secondary flow with increasing aspect ratio and Reynolds number, including its magnitude, convergence, and its impact on the statistics of the flow through the duct.

The present article is organized as follows: The numerical setup of the simulations is described in Sec. II; the topology of the secondary flow and its magnitude are described, for the various cases under consideration, in Secs. III and IV, respectively; turbulence statistics and wall-shear stress distributions are reported in Sec. V; and the main conclusions of this work are summarized in Sec. VI.

II. NUMERICAL SIMULATIONS

Turbulent duct flows with aspect ratios 1, 3, 5, 7, 10, and 14.4 at $\mathrm{Re}_{\tau,c} \simeq 180$, and with AR = 1 and 3 at $\mathrm{Re}_{\tau,c} \simeq 360$, were simulated by means of DNS. Note that part of this database has been previously reported [1,28], and that the AR = 14.4 case was designed to match the aspect ratio of one of the experiments in Ref. [29]. The simulations were performed with the code NEK5000, developed by Fischer *et al.* [30] and based on the spectral-element method (SEM) originally proposed by Patera [31]. In the SEM, the computational domain is decomposed into elements, and the solution is expressed in terms of Lagrange interpolants of order N within those elements. The location of the nodes inside the elements follows the Guass-Lobatto-Legendre (GLL) distribution, whereas there is an isoparametric mapping for the shape of the elements and there are no restrictions regarding the position of the elements in the domain. This means that this method allows the flexibility to compute complex geometries, while still preserving the characteristics of a high-order spectral method. In the present study, we considered the $\mathbb{P}_N - \mathbb{P}_{N-2}$ formulation with $N = 11$. Therefore, the velocity field was expressed in terms of Lagrange interpolants of order 11, and order 9 was considered for the pressure field. The nonlinear terms are treated explicitly by third-order extrapolation (EXT3), whereas the viscous terms are treated implicitly by a third-order backward differentiation scheme (BDF3). NEK5000 is written in FORTRAN 77 and C, and parallelized using a message-passing interface (MPI). Besides the already mentioned duct cases [1,15,28], we have used NEK5000 to simulate the turbulent flow through a straight pipe up to a moderately high friction Reynolds number of $\mathrm{Re}_\tau = 1{,}000$ [32]. During the runs, we computed a total of 71 statistical fields (where streamwise homogeneity was exploited), which were then used to calculate complete turbulence budgets. A complete description of the toolbox used to compute the turbulence statistics is given in Ref. [33].

With respect to the flow setup, periodicity is imposed in the streamwise direction x in all the cases, and no-slip conditions are imposed at the walls along the vertical and spanwise directions. All the ducts have a streamwise length of $L_x = 25h$, which is sufficiently long to simulate the most relevant turbulent structures in the flow [34,35], and the center-plane (at the plane $z/h = 0$) bulk Reynolds number $\mathrm{Re}_{b,c}$ (formed in terms of the center-plane bulk velocity $U_{b,c}$ and the duct half-height h) was kept approximately constant with AR by adjusting Re_b, as described by Vinuesa *et al.* [1]. The simulation parameters from all the cases are summarized in Table I, including mesh resolution details based on $u_{\tau,c}$, which fulfill all the standard requirements for a fully resolved DNS. The spectral elements are uniformly distributed in the homogeneous streamwise direction, and the range of Δx^+ values reported in Table I is due to the GLL point distribution within elements. The averaging periods t_a considered to obtain turbulence statistics (after the initial transients) are also reported in convective time units h/U_b and in eddy-turnover times $h/u_{\tau,c}$. All the simulations were initiated from a laminar solution [36], and transition to turbulence was triggered by means of a localized volume force acting in y. Its parameters were designed to create strong, unsteady streaks that lead to rapid turbulent breakdown [37]. Figure 2 shows an instantaneous streamwise velocity field obtained from the duct with AR = 10 at $\mathrm{Re}_{\tau,c} \simeq 180$. Near-wall streaks can be easily identified in this figure, with the well-documented spacing in the spanwise direction between two streaks of the same type (high- or low-speed) of $\lambda_z^+ \simeq 100$ [10,11]. The resolution is therefore appropriate to capture near-wall dynamics in the flow, and the use of a high-order method allows an appropriate

TABLE I. Summary of simulation parameters from the various cases, corresponding to $\mathrm{Re}_{\tau,c} \simeq 180$ (above) and $\mathrm{Re}_{\tau,c} \simeq 360$ (below) the horizontal line. The terms in brackets are the minimum and maximum grid spacing in that direction, respectively.

AR	Re_b	$\mathrm{Re}_{b,c}$	Re_τ	$\mathrm{Re}_{\tau,c}$	No. grid points	Δx^+	Δy^+	Δz^+	$t_a U_b/h$	$t_a u_{\tau,c}/h$
1	2500	2796	165	178	27.4×10^6	(1.98, 9.80)	(0.09, 4.74)	(0.09, 4.74)	7158	510
3	2581	2786	164	179	61.7×10^6	(1.99, 9.86)	(0.09, 4.77)	(0.09, 4.89)	5664	393
5	2592	2781	164	177	95.9×10^6	(1.97, 9.75)	(0.09, 4.72)	(0.09, 4.83)	6455	441
7	2605	2772	164	177	130.3×10^6	(1.97, 9.75)	(0.09, 4.72)	(0.09, 4.83)	9308	632
10	2580	2700	162	174	185.1×10^6	(1.93, 9.58)	(0.09, 4.64)	(0.09, 4.65)	5795	391
14.4	2665	2761	166	177	257.1×10^6	(1.97, 9.75)	(0.09, 4.72)	(0.09, 4.83)	3062	203
1	5693	6258	342	356	122.4×10^6	(1.99, 9.88)	(0.15, 4.65)	(0.15, 4.65)	3616	226
3	5817	6274	338	363	326.5×10^6	(2.03, 10.07)	(0.15, 4.75)	(0.15, 4.96)	3232	202

simulation of the turbulent velocity field. It is interesting to observe how near-wall streaks are also formed on the side walls, with an approximate spacing of $\lambda_y^+ \simeq 100$, and how at the corner the effect of the two walls inhibits the formation of such structures. Instead, the flow field in Fig. 2 shows how the bursting events from horizontal and vertical walls interact at the corner. As mentioned in Sec. I, these interactions were reported by Huser and Biringen [4] to result in a redistribution of energy from $\overline{v^2}$ to $\overline{w^2}$ in square ducts, which eventually leads to the formation of the mean secondary flow.

III. TOPOLOGY OF THE SECONDARY FLOW

The evolution of the secondary flow topology with Reynolds number and aspect ratio is presented in Fig. 3, where the streamlines of the secondary mean flow Ψ are evaluated from the two-dimensional fields obtained after averaging in the streamwise direction and in time, as well as over the four quadrants in the duct. Figure 3 (top) shows the streamlines from square ducts at $\mathrm{Re}_{\tau,c} \simeq 180$ and $\mathrm{Re}_{\tau,c} \simeq 360$, with the characteristic two-vortex pattern on each corner and the tangent line between the vortices along the corner bisector. It can be observed that the secondary vortices convect momentum from the duct center plane toward the bisector and that the two vortices are symmetric with respect to their tangent line at a particular Reynolds number. This figure illustrates the findings

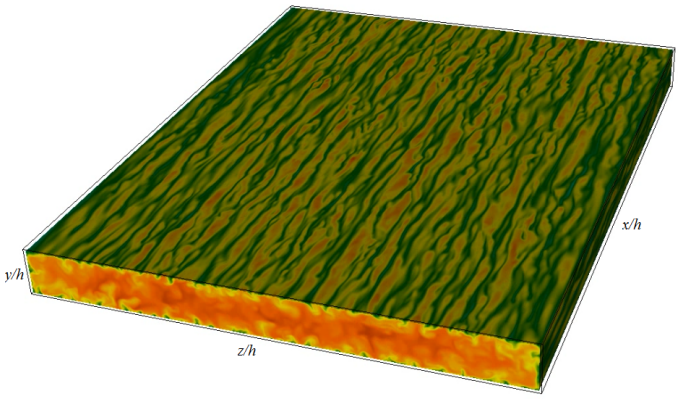

FIG. 2. Instantaneous streamwise velocity field in the AR = 10, $\mathrm{Re}_{\tau,c} \simeq 180$ case at 2000 convective time units (normalized with U_b and h) from the beginning of the simulation. Green and orange represent minimum and maximum velocities in the field, respectively. Flow is from lower left to upper right, and walls have been made transparent for clarity.

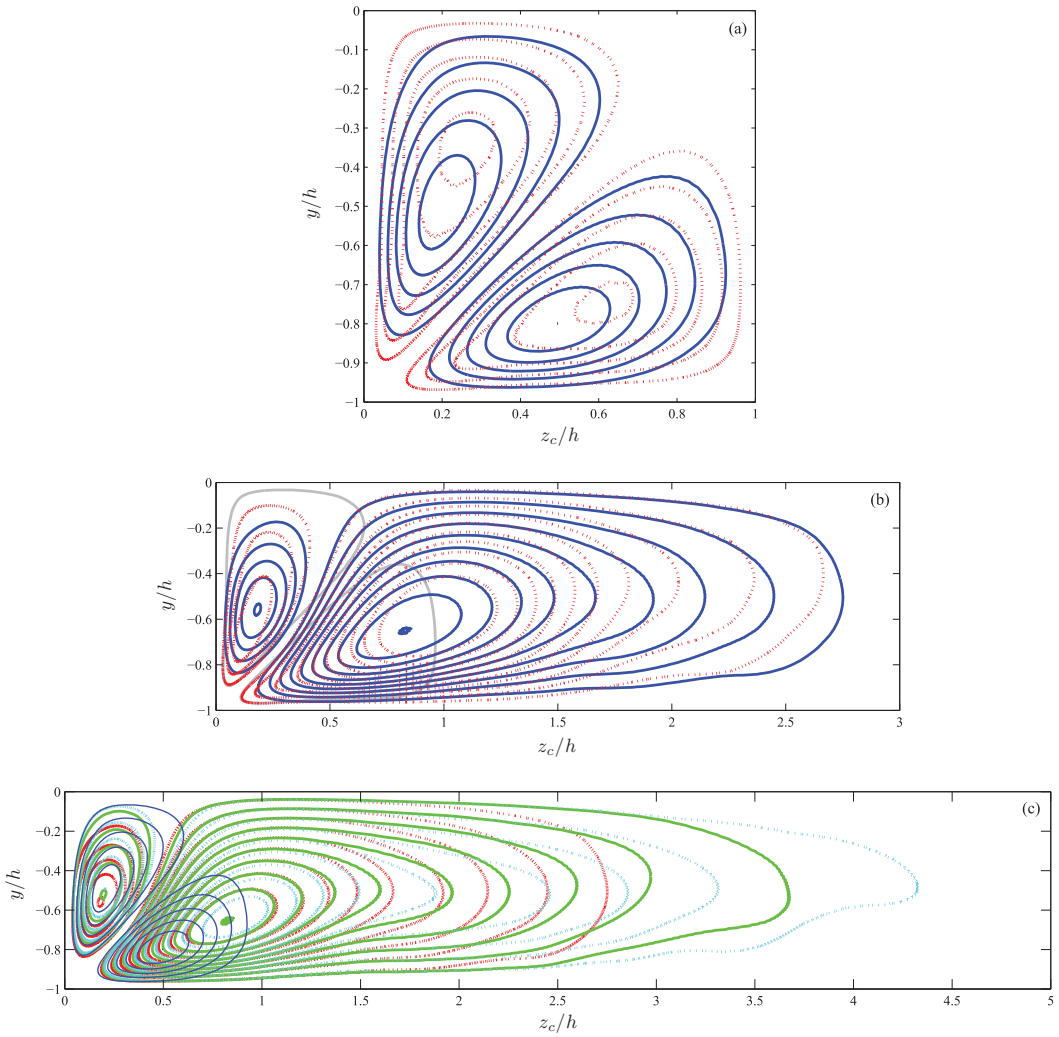

FIG. 3. Streamlines of secondary mean flow Ψ, where the coordinate z_c is defined with its origin at the duct corner. (a) Square ducts at ——— $\mathrm{Re}_{\tau,c} \simeq 180$ and ····· $\mathrm{Re}_{\tau,c} \simeq 360$; (b) AR = 3 ducts at ——— $\mathrm{Re}_{\tau,c} \simeq 180$, ····· $\mathrm{Re}_{\tau,c} \simeq 360$ and ——— shows the first contour (with value 3.9×10^{-4}) from the square duct at $\mathrm{Re}_{\tau,c} \simeq 360$ for comparison; (c) $\mathrm{Re}_{\tau,c} \simeq 180$ ducts with ——— AR = 1, ····· AR = 3, ——— AR = 5, and ····· AR = 10. A total of 10 contours are shown in the square duct cases, whereas 15 are shown in the wider ducts, all of them with increments of 3.9×10^{-4}. The velocity and length scales are, respectively, U_b and h.

by Pinelli *et al.* [9] in their numerical work on square ducts up to $\mathrm{Re}_\tau = 225$: As Re increases, the secondary vortices become more elongated and their centers move away from the wall. An extension of this analysis to rectangular ducts is presented in Fig. 3 (middle), where the secondary flow streamlines from the AR = 3 cases at $\mathrm{Re}_{\tau,c} \simeq 180$ and 360 are compared. In this figure, we show a total of 15 contours, with the same increments as in the square-duct cases (3.9×10^{-4}), in order to allow better comparison among the various ducts. Also in these wider ducts two counter-rotating vortices are observed close to the corner, although the symmetry they exhibited in the square duct is lost: The vortex located on the horizontal wall significantly expands in the spanwise direction, which leads to the fact that the tangent line between the two vortices is not straight anymore and

does not follow the corner bisector. The spanwise development of the vortex on the horizontal wall leads to an increase in its vertical size, with the consequent shrinking of the vortex on the vertical wall; therefore the tangent line is a concave curve connecting the lower-left corner and the point ($z_c/h \simeq 0.5, y/h \simeq 0$). Regarding the vortex on the horizontal wall, the first contour extends to the corner up to the same z_c/h values as the square duct (0.18 and 0.1 for low and high Re, respectively), which indicates that the corner has an important influence in the formation of the secondary vortex. The development of this vortex in the spanwise direction is similar for the two Reynolds numbers, and in both cases the last contour (with a value of 3.9×10^{-3}) extends up to z_c/h values slightly above 2.5; i.e., the secondary flow is observed up to spanwise locations close to the center plane. The center of this vortex also moves farther from the wall with Re: In the low-Re case it is located at ($z_c/h \simeq 0.80$, $y_c/h \simeq 0.35$), and in the higher Re this center is at ($z_c/h \simeq 1$, $y_c/h \simeq 0.4$), which supports the notion of large-scale motions influencing the development of the secondary vortices. With respect to the vortex on the vertical wall, vertical stretching is also observed with increasing Re, and in both cases the vortex becomes compressed horizontally due to the discussed growth of the vortex on the horizontal wall. The first contour from the square duct at $\mathrm{Re}_{\tau,c} \simeq 360$ is shown for comparison, where the shrinking of this vortex is noticeable, although interestingly this first contour is similarly close to the corner, reinforcing its high influence in the secondary flow. Despite the fact that the higher Re vortex is more elongated, its center is approximately at the same location as that of the low-Re case.

An assessment of the influence of the aspect ratio on the topology of the secondary vortices is presented in Fig. 3 (bottom). Analysis of aspect ratios of 1, 3, 5, and 10, at $\mathrm{Re}_{\tau,c} \simeq 180$, leads to some similar observations compared with Fig. 3 (middle), in particular the fact that the vortex on the vertical wall shrinks horizontally and the tangent line, also defined by a concave curve connecting the lower left corner and the point ($z_c/h \simeq 0.5, y/h \simeq 0$), is very similar in all the aspect ratios. Regarding the horizontal wall, the first contour level is in good agreement close to the corner in all the aspect ratios, and interestingly is almost identical in aspect ratios 3, 5, and 10 up to $z_c/h \simeq 1.75$. The similarities in this first contour persist for the AR = 5 and 10 cases up to $z_c/h \simeq 2.5$, point after which the vortex extends up to $z_c/h \simeq 3.7$ in the aspect ratio 5 case, and up to $z_c/h \simeq 4.3$ in the wider duct. This indicates that the secondary flow develops a characteristic pattern in rectangular ducts, and although the features change close to the center plane as the aspect ratio becomes higher, the vortices exhibit similar features close to the corner. This claim is further supported by the fact that the center of the secondary vortex on the horizontal wall is approximately at the same location in all the aspect ratios larger than 1, i.e., at ($z_c/h \simeq 0.80$, $y_c/h \simeq 0.35$). The horizontal shrinking of the vortex on the vertical wall can be observed in comparison with the square duct, although as already discussed in Fig. 3 (middle), the first contour level is similar in all the cases, even in the square duct, close to the corner. With respect to the vertical extent, the vortex in the AR = 3 duct is slightly shorter, which could be associated with some intermediate state of development of the secondary flow as AR increases, since the vortices from the wider ducts are almost identical. It is also interesting to note that the center of this vortex is approximately at the same location in all the cases: ($z_c/h \simeq 0.2$, $y_c/h \simeq 0.5$).

The evolution of the secondary flow with increasing Reynolds number, as well as with increasing aspect ratio, indicates that the large-scale motions in the flow are strongly related to its origin and development, as observed by Pinelli *et al.* [9] in square ducts. The novelty of these results lies in the fact that larger scales arising from the wider spanwise extent also affect significantly the shape of the secondary vortices, as well as their intensity.

IV. MAGNITUDE OF THE SECONDARY FLOW

After discussing the topology of the secondary flow in the various duct cases, in this section we quantify its magnitude in terms of the cross-flow kinetic energy $K = 1/2(V^2 + W^2)$ at various locations in the spanwise direction z. The mean wall-normal and spanwise velocity components V and W are normalized with the bulk velocity U_b, and therefore K is normalized with U_b^2 throughout the article. Figure 4 (top) shows the K distribution of the AR = 3 case at $\mathrm{Re}_{\tau,c} \simeq 180$, which exhibits

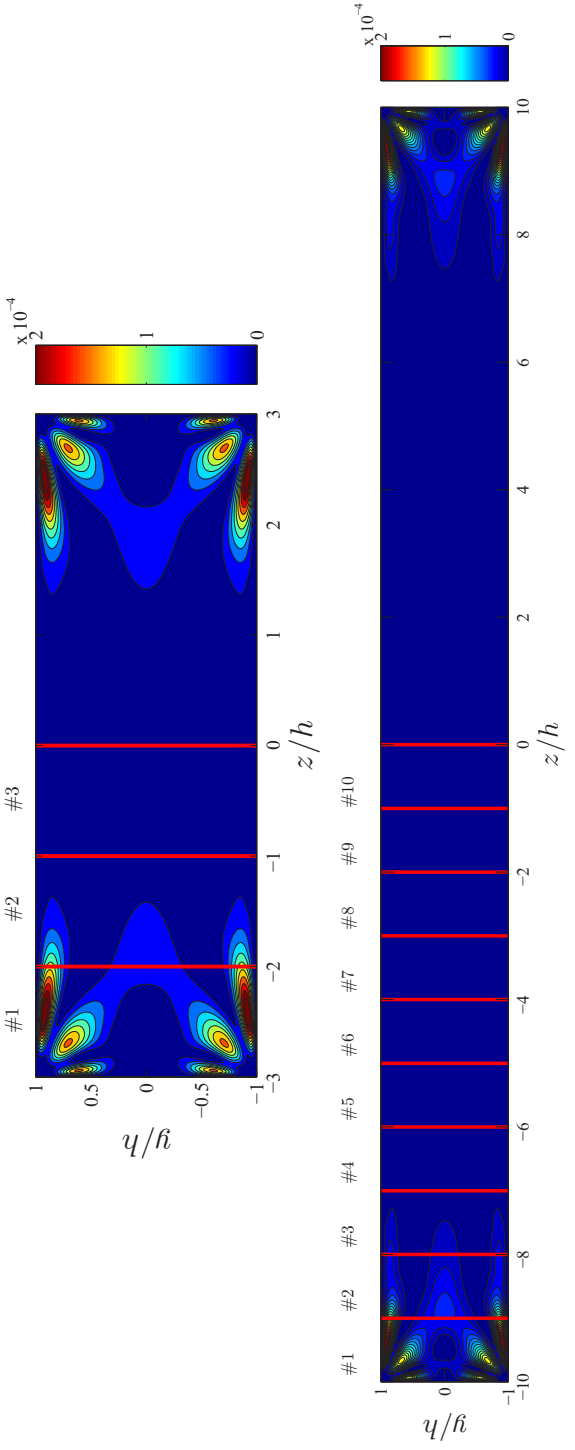

FIG. 4. Kinetic energy of the secondary flow K for the (top) AR $= 3$ and (bottom) AR $= 10$ cases at $\mathrm{Re}_{\tau,c} \simeq 180$, together with the windows used to calculate $\langle K \rangle_{yz}$. Fields obtained after averaging in the streamwise direction, time, and over the four duct quadrants.

high energy close to the corner on the horizontal wall, associated with the strength of the secondary vortex in that region. Note that in this figure we exploited the flow symmetries to improve the statistics. Although in Fig. 3 it could be observed that the streamlines of the secondary flow extend beyond $z_c/h \simeq 2.5$, Fig. 4 (top) shows that the energy level of the secondary flow is low for $z_c/h > 1.5$ approximately. Another region of high K corresponds to the vertical motion parallel to the vertical wall, and the third region with high kinetic energy is precisely the tangent line between the two corner vortices, directed toward the corner. Regarding the AR $= 10$ case at $\mathrm{Re}_{\tau,c} \simeq 180$ shown in Fig. 4 (bottom), similar regions of high K can be identified, i.e., parallel to the horizontal and vertical walls, and along the tangent lines between the two corner vortices. Although Fig. 3 shows that the streamlines extend up to $z_c/h \simeq 4.3$, according to the energy distribution from Fig. 4 the magnitude of the secondary flow decays significantly beyond $z_c/h \simeq 3$. A difference in energy distribution between the AR $= 3$ and 10 cases can be observed close to the corner, at $y/h \simeq 0$: Whereas in the narrower duct a region of intermediate energy can be observed up to $z_c/h \simeq 1.5$, this area extends up to $z_c/h \simeq 2.5$ in the wider case. This is related to the discrepancy in streamlines from Fig. 3 (bottom) beyond $z_c/h \simeq 1.75$, and it can be explained by the fact that the larger width allows further development of the secondary flow in the AR $= 10$ case, thus modifying its energy distribution.

Because of the spanwise inhomogeneity of the duct, it is not possible to average the flow in the spanwise direction when computing turbulence statistics, as it is done in spanwise-periodic channels [38–40]. As a result, longer averaging times are in principle required to obtain converged statistics in turbulent ducts than in turbulent channels. In the present study, we divide the rectangular ducts into smaller areas of width h and height $2h$, which we denote by "windows." Consequently, the square duct would be divided into two windows, and the AR $= 10$ case into 20. The symmetry of the flow with respect to the $z/h = 0$ plane is used to improve the statistics, which leads to a total of 10 windows in the AR $= 10$ case. The division into windows is illustrated for the AR $= 3$ and 10 cases at $\mathrm{Re}_{\tau,c} \simeq 180$ in Fig. 4. As a convention, we will denote the window closest to the corner as no. 1, and increase the number up to the value of the one closer to the core of the duct. For instance, in the aspect ratio 10 case the window from $z/h = -10$ to -9 would be no. 1, and the one from $z/h = -1$ to 0 would be no. 10. In order to determine the required averaging periods to obtain converged secondary flow statistics, the evolution of K with t_a is characterized for each of the windows. Doing so, it will be possible to determine their respective rates of convergence and converged values. We will use the symbol $\langle\cdot\rangle$ to denote the spatial average of a certain quantity, whereas capital letters denote the mean in time.

The convergence of the secondary flow is evaluated, for the first window (as described in Fig. 4), in Fig. 5 for all the aspect ratios at $\mathrm{Re}_{\tau,c} \simeq 180$. In this figure, we show the value of K averaged over the first window, i.e., $\langle K\rangle_{yz1}$, as a function of the averaging time $t_a U_b/h$ (expressed in convective time units), where also streamwise averaging, as well as averaging over the two symmetric windows, were considered. All the aspect-ratio cases reach a fully converged state after approximately 3000 convective time units, a fact that highlights the long averaging periods required for the secondary flow to converge. The square duct shows the lowest level of energy once the converged state is reached: $\langle K\rangle_{yz1} \simeq 3\times10^{-5}$, whereas aspect ratios 3 and 5 exhibit values of around 4.5×10^{-5}. The higher aspect ratios 7, 10, and 14.4 have a slightly lower $\langle K\rangle_{yz1}$ value of 4×10^{-5}. These differences are explained by the spanwise development of the secondary flow: The square duct does not allow the cross flow to evolve and reach the form it would exhibit in a sufficiently wider duct. With respect to aspect ratios 3 and 5, they show a pattern closer to the wider 7 and 10 cases, but constrained to a narrower space, which leads to higher concentration of energy close to the corner. Analysis of $\langle K\rangle_{yz1}$ in the two cases at $\mathrm{Re}_{\tau,c} \simeq 360$ (not shown) reveals that around 3000 convective time units are also required for the secondary flow to converge. Moreover, the $\langle K\rangle_{yz1}$ values are almost identical when compared with those at $\mathrm{Re}_{\tau,c} \simeq 180$ for the two aspect ratios, as shown in Table II. Despite the topological differences observed in the secondary flow with increasing Reynolds number, already discussed in Fig. 3, it appears that the integrated value of K is not significantly affected by Re, at least close to the corner. This observation, limited to a narrow Reynolds-number range, also indicates that the secondary flow scales in outer units, i.e., with the bulk velocity U_b. This conclusion is in

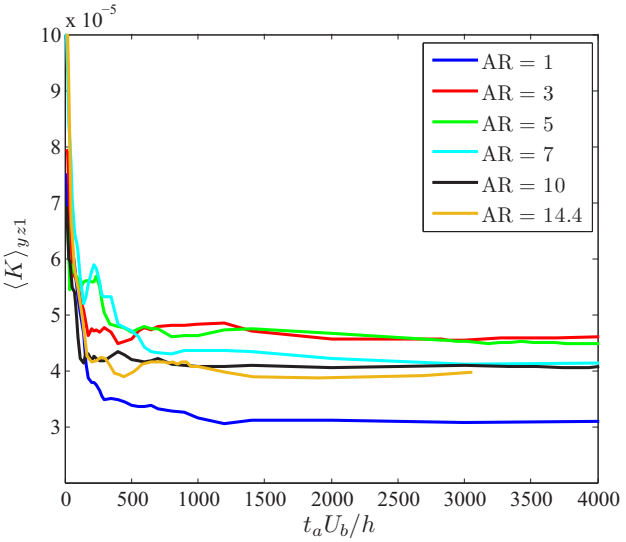

FIG. 5. Kinetic energy of the secondary flow averaged over the first window $\langle K \rangle_{yz1}$ as a function of averaging time, for all the aspect ratios at $\mathrm{Re}_{\tau,c} \simeq 180$.

agreement with the recent work by Pirozzoli *et al.* [19], who performed DNS of turbulent square duct flow up to $\mathrm{Re}_\tau \simeq 1000$. In this study, it is also shown that the secondary flow scales with U_b over their Re range.

The previous analysis of the first window is extended in Fig. 6 to windows 2 and 3, which excludes the square ducts. The $\mathrm{Re}_{\tau,c} \simeq 180$ cases presented in Fig. 6 show that the second window exhibits in all the ducts a very similar converged level of energy (after averaging for at least 3000 time units) of $\langle K \rangle_{yz2} \simeq 2\times10^{-5}$, which suggests that beyond a certain width the secondary flow, initiated at the corner, shares common features in all the ducts. Interestingly, the third window from aspect ratios 5, 7, 10, and 14.4 show a very similar level of energy $\langle K \rangle_{yz3} \simeq 5\times10^{-6}$, whereas the energy corresponding to the AR = 3 case is lower: 2.5×10^{-6}. This can be justified by the fact that in the AR = 3 case the third window corresponds to the one at the center plane, and as observed in the topology of the secondary flow from Fig. 3, and the distribution of K from Fig. 4, the secondary flow is already almost absent in the third window. Nevertheless, the wider ducts allow further penetration of the secondary flow into their respective cores, exhibiting again similar features in this development, illustrated in the levels of $\langle K \rangle_{yz3}$. Regarding windows 2 and 3 at $\mathrm{Re}_{\tau,c} \simeq 360$, they also exhibit converged secondary flow after averaging for around 3000 convective time units (not shown). As

TABLE II. Converged values of $\langle K \rangle_{yz}$ in windows 1, 2, and 3 for the various cases under consideration.

AR	$\mathrm{Re}_{\tau,c}$	$\langle K \rangle_{yz1}$	$\langle K \rangle_{yz2}$	$\langle K \rangle_{yz3}$
1	178	3.0×10^{-5}		
3	179	4.5×10^{-5}	2.0×10^{-5}	2.5×10^{-6}
5	177	4.5×10^{-5}	2.0×10^{-5}	5.0×10^{-6}
7	177	4.0×10^{-5}	2.0×10^{-5}	5.0×10^{-6}
10	174	4.0×10^{-5}	2.0×10^{-5}	5.0×10^{-6}
14.4	177	4.0×10^{-5}	2.0×10^{-5}	5.0×10^{-6}
1	356	3.1×10^{-5}		
3	363	4.7×10^{-5}	2.5×10^{-5}	2.0×10^{-6}

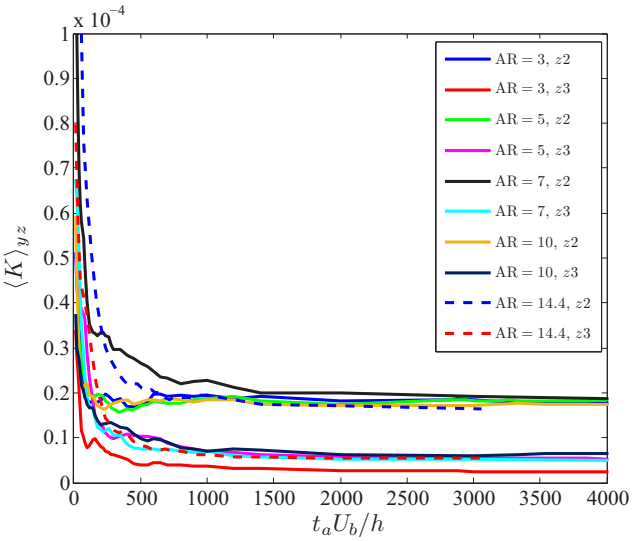

FIG. 6. Kinetic energy of the secondary flow averaged over the second and third windows as a function of averaging time. Cases as in Fig. 5, excluding the square duct.

expected, the third window exhibits values much lower than the second one in the two cases, slightly lower in the higher Re case: 2×10^{-6}. On the other hand, although the second window exhibits similar levels of energy with Re, a slight increment from $\langle K\rangle_{yz2} \simeq 2\times10^{-5}$ to $\langle K\rangle_{yz2} \simeq 2.5\times10^{-5}$ is found when $\mathrm{Re}_{\tau,c}$ increases. This is interesting, since the AR $= 3$ duct did not exhibit significantly larger energy in the first window (only an increase of around 4.4%), whereas in the second one the integrated K is around 25% higher. The stream function from both cases, shown in Fig. 3 (middle), shows how in the higher Re duct the streamlines appear to be slightly more concentrated in the second window, which would explain the higher value of $\langle K\rangle_{yz2}$ and the lower one of $\langle K\rangle_{yz3}$. Moreover, the center of the vortex on the horizontal wall is displaced toward $z_c/h \simeq 1$ at $\mathrm{Re}_{\tau,c} \simeq 360$, which is a consequence of the larger contributions from the large-scale motions of the flow, and could also be related to the higher level of energy in the second window. Nevertheless, we do not observe a significantly different mechanism in the spanwise development of the secondary flow at this higher Re. The converged values of $\langle K\rangle_{yz}$ in windows 1, 2, and 3 for the various cases are summarized in Table II.

The energy level of the secondary flow at the core of the duct is characterized for the aspect ratios AR $= 7$, 10, and 14.4, all of them at $\mathrm{Re}_{\tau,c} \simeq 180$, in Fig. 7. For this analysis, we consider windows larger than or equal to window 6, which implies that we consider two windows in the aspect ratio 7 case, and a total of nine windows in AR $= 14.4$ (since in this case the 15th window would have a width of only $0.4h$, we decided to exclude it from this figure). In addition to these, we also show the results of a channel flow simulation (where spanwise periodicity was imposed), performed with the Fourier-Chebyshev spectral code SIMSON [41], in a computational domain with same streamwise length as the duct cases ($L_x = 25h$) and with a ratio between spanwise and wall-normal lengths $L_z/L_y = 5$. For the channel results, we considered a single window spanning the whole width of the periodic domain, although the same trend is obtained by assuming windows of different sizes. This particular choice of windows to define the core of the duct was motivated by Figs. 3 (bottom) and 4 (bottom), which show that the secondary flow is significantly attenuated beyond window 5. The value of $\langle K\rangle_{yz}$ decays as the averaging time increases in all the windows and in the channel, and both flows exhibit the same rate of decay $\langle K\rangle_{yz} \sim t_a^{-1}$; note that this rate of decay has already been observed in the literature [28]. This suggests that, at the core, K is in fact a random variable with zero mean. Thus, increasing the averaging time (or the number of statistical samples) produces

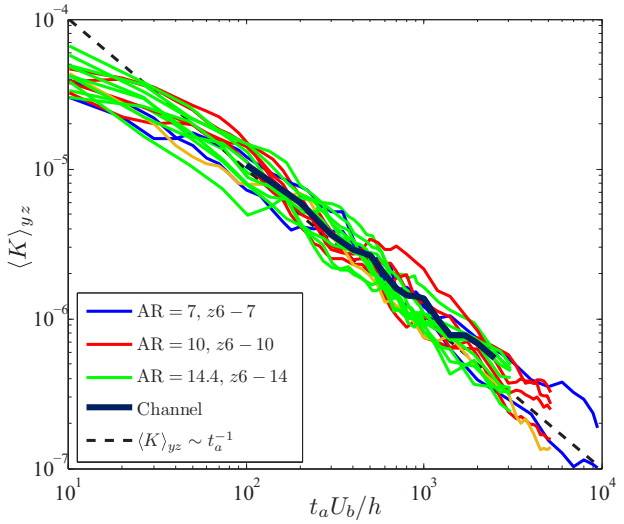

FIG. 7. Kinetic energy of the secondary flow averaged over windows larger than or equal wo window 6, as a function of averaging time, for AR = 7, 10, and 14.4 at $\mathrm{Re}_{\tau,c} \simeq 180$. The same quantity is shown averaged over the cross-sectional area in a spanwise-periodic channel, together with the observed rate of decay $\langle K \rangle_{yz} \sim t_a^{-1}$.

a decreasing trend. Also note that the rate of convergence of V and W is $\sim t_a^{-1/2}$, which is consistent with the central limit theorem and is a result independent of the aspect ratio. It is also interesting to observe that all the windows from the various aspect-ratio cases exhibit similar K values after averaging for comparable time intervals. Figure 7 shows that the long-time average of the cross flow in a spanwise-periodic channel and in the core of a sufficiently wide duct are similar.

The fourth and fifth windows are analyzed for aspect ratios 5, 7, 10, and 14.4, all of them at $\mathrm{Re}_{\tau,c} \simeq 180$, in Fig. 8. It is interesting to note that although the levels of energy from the various cases do not decay at the rate $\langle K \rangle_{yz} \sim t_a^{-1}$, it is not clear whether the data would converge to a nonzero value or not. In any case, the behavior in this region is different from the one observed at the core, where the rate of decay is consistent with the one exhibited by a spanwise-periodic channel, and therefore it can be stated that in windows 4 and 5 the flow does not behave as it does in the channel. The fourth window exhibits the same trend in AR = 7, 10, and 14.4, with higher energy level than the corresponding window in the AR = 5 duct. Although in general the rate of decay from the fifth window is steeper in all the cases than that of the fourth one, also in this case AR = 5 is the one below all the other ducts. This is in agreement with the discussion from Fig. 6, where the third window in the AR = 3 duct exhibited significantly lower levels of energy, due to the fact that the secondary flow was not allowed to further expand in the spanwise direction due to the limited width. These results suggest that although the magnitude of the secondary flow in the region $4 < z/h < 5$ is smaller than the one observed closer to the corner, the behavior in this section of the duct is not the same as the one observed in spanwise-periodic channels.

After assessing the levels of energy associated with the secondary flow at localized regions in the duct, we evaluate the spanwise variation of the kinetic energy averaged over the wall-normal direction $\langle K \rangle_y$. Figure 9 shows this quantity for all the ducts at $\mathrm{Re}_{\tau,c} \simeq 180$, and here we also consider the variable z_c with its origin at the corner. In Fig. 9 (left), we focus on the region close to the corner, which as highlighted above shows a stronger secondary flow that becomes gradually attenuated as the core of the duct is approached. The two local maxima and the minimum identified in the region close to the corner can be connected with the topology of the secondary flow shown in Fig. 3, and the K distribution from Fig. 4: The first maximum in $\langle K \rangle_y$, located at $z_c/h \simeq 0.06$, is associated with the region of high energy due to the vertical motion, parallel to the side wall, from the first secondary

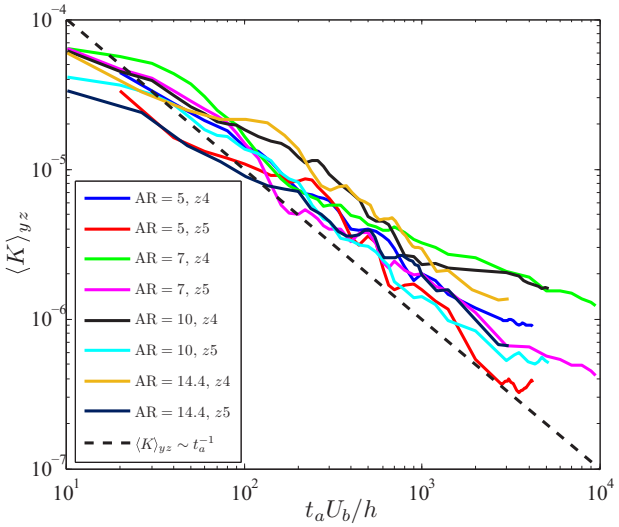

FIG. 8. Kinetic energy of the secondary flow averaged over the fourth and fifth windows as a function of averaging time. Cases as in Fig. 5, excluding the AR = 1 and 3 ducts, and rate of decay $\langle K \rangle_{yz} \sim t_a^{-1}$ shown for comparison purposes.

vortex. Note that the location of this peak is invariant with aspect ratio, and its magnitude depends on the constraining effect of the aspect ratio, as will be discussed below. The second maximum, which is located at $z_c/h \simeq 0.4$ in all the cases except the square duct (where it is slightly closer to the corner, at $z_c/h \simeq 0.3$), is associated with the region of high K arising from the horizontal motion, parallel to the wall, of the second vortex. The local minimum, which again exhibits an invariant position with AR equal to $z_c/h \simeq 0.18$, approximately corresponds to the center of the vortex on the vertical wall, where the energy level is lower. This is also noticeable in the K distributions from Fig. 4, where it is evident that this local minimum is located between the region of high K associated with the vertical and the horizontal motions. Note that although all the aspect ratios show a similar structure, with

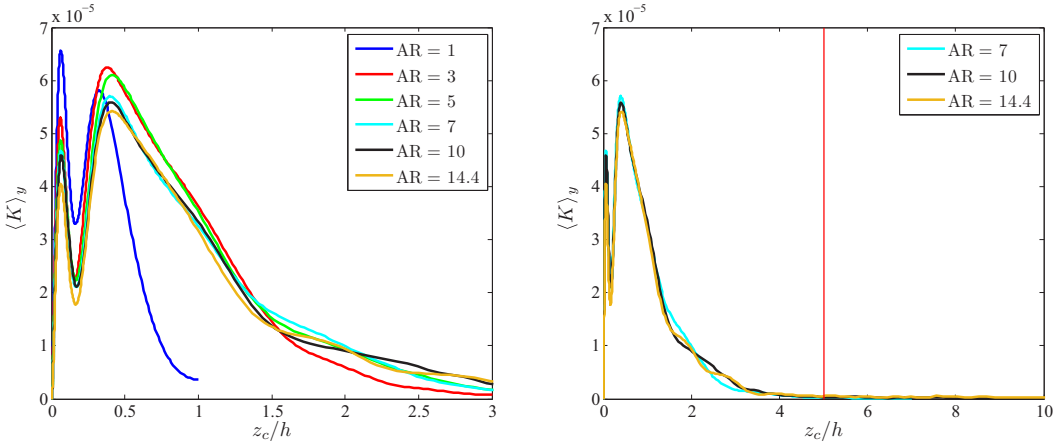

FIG. 9. Spanwise variation of the kinetic energy of the secondary flow averaged over the wall-normal direction $\langle K \rangle_y$, for all the duct cases at $\mathrm{Re}_{\tau,c} \simeq 180$. The left panel shows the region close to the corner, whereas in the right panel we focus on the aspect ratios larger or equal than 7 and show a wider spanwise extent.

TABLE III. Total kinetic energy of the secondary flow for the various cases under consideration.

AR	$\mathrm{Re}_{\tau,c}$	K_{total}
1	178	6.0×10^{-5}
3	179	13.1×10^{-5}
5	177	13.8×10^{-5}
7	177	13.3×10^{-5}
10	174	13.4×10^{-5}
14.4	177	13.4×10^{-5}
1	356	6.2×10^{-5}
3	363	15.1×10^{-5}

two local maxima and one local minimum in between, their actual values are strongly influenced by the constraining effect of the aspect ratio. Thus, AR determines the structure of the secondary flow, where, for instance, it is clear that the square duct exhibits a higher concentration of energy close to the corner and has a steeper decay of kinetic energy as the center plane is approached. This is also consistent with Fig. 5, where we show that the integrated value of K over that first window is lower in the square duct and provides additional support to the claim that the duct develops similar features in all the aspect ratios if the width is large enough. The significantly larger maximum of $\langle K\rangle_y$ close to the corner in the square duct (between 30% and 44% larger than the other cases) is also remarkable. It is also interesting to observe that the aspect ratio 7 and 10 cases exhibit a similar peak value of $\langle K\rangle_y$ close to the corner, whereas AR $= 3$ and 5 show intermediate values, highlighting the developing nature of the secondary flow with AR. The widest duct exhibits slightly lower values in the first maximum, and also in the minimum, than the other cases. The ducts with aspect ratios 3 and 5 also show larger values in the second maximum than the cases with AR $= 7$, 10, and 14.4. This can be explained by the fact that the secondary flow extends up to $z_c/h \simeq 5$, and if the duct is not wide enough to accommodate the whole extent of the secondary flow, then its structure is modified by means of a different spanwise distribution of energy. Further insight on these distributions can be gained by analyzing the values reported in Table III, where the total kinetic energy of the secondary flow K_{total}, defined as

$$K_{\mathrm{total}} = \int_{y/h=-1}^{y/h=1}\int_{z/h=-\mathrm{AR}}^{z/h=\mathrm{AR}} K\, d(y/h)d(z/h), \tag{1}$$

is reported for all the duct cases. Focusing now on $\mathrm{Re}_{\tau,c} \simeq 180$, the square duct shows the lowest total energy level, more than a factor of 2 below the AR $= 3$ case. This is not surprising, since the already mentioned constraining effect of the duct width does not allow the spanwise development of the secondary flow. Moreover, there are small differences among the cases with AR $\geqslant 3$, where the AR $= 3$ duct is slightly below the others (manifested in the $\langle K\rangle_y$ curve, which is slightly below the other cases for $z_c/h > 1.5$) and the AR $= 5$ slightly above (mostly noticeable in the larger peak of $\langle K\rangle_y$ at $z_c/h \simeq 0.4$). Beyond this aspect ratio, all the cases exhibit a very similar total energy of $K_{\mathrm{total}} \simeq 13.4\times10^{-5}$, which again supports the statement that for sufficiently wide ducts the secondary flow reaches a limited and defined spanwise development. The fact that the total energy of the secondary flow appears to be constant beyond a certain aspect ratio could explain the small decay observed in the three relative extrema of $\langle K\rangle_y$ with increasing aspect ratio. Moreover, the notion that the secondary flow is stronger close to the corner and becomes gradually attenuated as the core of the duct is approached is also observed in Fig. 9 (right), where $\langle K\rangle_y$ is shown as a function of z_c for the aspect ratio 7, 10, and 14.4 cases, in the region $0 \leqslant z_c/h \leqslant 10$. Here it also becomes clear that the corner effects are relevant up to the fifth window, and beyond this point they basically become zero when long averaging times are considered.

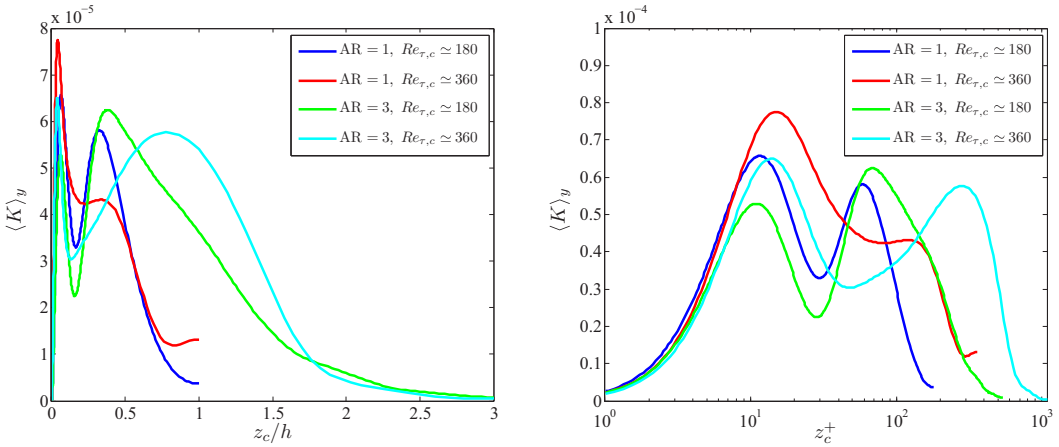

FIG. 10. Spanwise variation of the kinetic energy of the secondary flow averaged over the wall-normal direction $\langle K \rangle_y$, for the AR $= 1$ and 3 cases at $\mathrm{Re}_{\tau,c} \simeq 180$ and 360. In the left panel, the z_c coordinate is scaled in outer units, whereas in the right one inner scaling is considered.

The effect of Reynolds number on the $\langle K \rangle_y$ distributions is assessed in Fig. 10, where the AR $= 1$ and 3 cases are compared at $\mathrm{Re}_{\tau,c} \simeq 180$ and 360. We first consider the spanwise coordinate z_c in outer scaling [Fig. 10 (left)], which shows that at $\mathrm{Re}_{\tau,c} \simeq 360$ the first maximum in $\langle K \rangle_y$, associated with the energetic vertical motion along the vertical wall, is located closer to the side wall than at $\mathrm{Re}_{\tau,c} \simeq 180$, i.e., at $z_c/h \simeq 0.04$ instead of 0.06. This is explained by the fact that as shown in Fig. 3, the secondary vortices on the vertical wall become more elongated vertically and are slightly more constrained in the region close to the side wall. Moreover, the value of the peak increases with Re, which is connected with larger vertical velocities, a consequence of the compression of the vortex toward the side wall. Regarding the local minimum, it is interesting to observe that at $\mathrm{Re}_{\tau,c} \simeq 360$ the square duct exhibits a plateau at around $z_c/h \simeq 0.22$, whereas the AR $= 3$ duct shows a minimum at $z_c/h \simeq 0.13$; let us recall that in the lower Re case the minimum lies in between, at $z_c/h \simeq 0.18$. This minimum is connected with the center of the vortex located at the vertical wall, combined with the fact that at $\mathrm{Re}_{\tau,c} \simeq 180$ the two aspect ratios show a similar $\langle K \rangle_y$ around it, whereas at $\mathrm{Re}_{\tau,c} \simeq 360$ not only the minima are located in different places but also the slopes of $\langle K \rangle_y$ are different before and after the mentioned minimum, suggests that different mechanisms associated with the larger scales produce a different secondary flow development. Regarding the second maximum, its location in the square duct at $\mathrm{Re}_{\tau,c} \simeq 360$ is approximately the same as in the two lower Re cases, i.e., $z_c/h \simeq 0.4$. The value of this peak is 25% lower than that of the square duct at $\mathrm{Re}_{\tau,c} \simeq 180$. This can be explained by the fact that, as shown in Table III, the total energy of the secondary flow is approximately the same in the two square ducts, and since the first peak is significantly larger at $\mathrm{Re}_{\tau,c} \simeq 360$, the second one must necessarily diminish. From a topological point of view, the fact that the secondary vortex on the horizontal wall is significantly more elongated at higher Re (as observed in Fig. 3), indicates that the high-speed region on the wall is spread over a wider distance in z, therefore leading to the plateau observed in $\langle K \rangle_y$ for this case. With respect to AR $= 3$, the second maximum is significantly farther from the corner, at $z_c/h \simeq 0.8$, and although the peak value is slightly below that of the AR $= 3$ case at $\mathrm{Re}_{\tau,c} \simeq 180$, the higher Re case exhibits larger values of $\langle K \rangle_y$ over a wider spanwise distance. This is connected to the larger K_{total} value reported in Table III and justified by the topology of the horizontal secondary vortex, as observed in Figure 3: The development of this vortex compared with the lower Reynolds number shows that the streamlines are closer together toward the horizontal wall, which leads to higher acceleration of the flow in the z_c direction, and consequently to higher K over a longer spanwise distance. Further insight on the Reynolds-number effects can be gained by analyzing the $\langle K \rangle_y$ curves with the z_c coordinate scaled in wall units, as shown in Fig. 10 (right): Interestingly,

TABLE IV. Summary of 99% side-wall boundary-layer thicknesses $\delta_{99,z}$ for the various cases under consideration.

AR	$\mathrm{Re}_{\tau,c}$	$\delta_{99,z}/(W_d/2)$	$\delta_{99,z}/h$
1	178	0.84	0.84
3	179	0.70	2.11
5	177	0.70	3.48
7	177	0.67	4.71
10	174	0.50	4.99
14.4	177	0.38	5.48
1	356	0.85	0.85
3	363	0.78	2.34

the first maxima are now at a very similar distance to the corner in inner units, i.e., at $z_c^+ \simeq 12$ and 15 for the low- and high-Re cases, respectively. This highlights the strong connections of the vertical secondary motion with near-wall turbulent events. The local minimum (connected with the center of the vortex on the vertical wall) from the low-Re cases appeared to be located at a distance from the corner right between the one from the AR = 3 and AR = 1 cases at high Re, when scaled in outer units. Nevertheless, inner scaling reveals that the two low-Re cases show this minimum at $z_c^+ \simeq 30$, the square duct at high Re at $z_c^+ \simeq 80$, and the AR = 3 case at $z_c^+ \simeq 46$. This behavior suggests that the contributions from both small- and large-scale motions are extremely relevant in the development of the secondary vortices (both with Re and AR), as also observed by Pinelli *et al.* [9]. Finally, inner scaling also reveals an interesting trend of the second maximum: The two $\mathrm{Re}_{\tau,c} \simeq 180$ cases show it at $z_c^+ \simeq 70$, and whereas the square duct at higher Re showed it at the same outer-scaled location, in inner scaling this maximum is observed at $z_c^+ \simeq 130$; the wider ducts show this peak at an even larger distance from the corner of $z_c^+ \simeq 280$. To conclude, despite the similarities in the development of the secondary flow as the ducts become wider and Reynolds number is increased, the complex multiscale nature of these vortices leads to interesting differences observed in the particular cases, especially as both the Reynolds number and the aspect ratio are increased.

Besides the secondary flow, another interesting three-dimensional effect present in rectangular ducts is the growth and development of side-wall boundary layers. In the present work, we evaluated the side-wall boundary-layer thickness at the $y = 0$ plane, and in order to avoid ambiguous definitions of δ, we considered the 99% boundary-layer thickness $\delta_{99,z}$, defined as the z position where $U = 0.99U_c$ [where U_c is the centerline velocity, i.e., $U_c = U(y/h = z/h = 0)$]. The values of $\delta_{99,z}$ are summarized for the various cases in Table IV, where scalings with the duct half-width $W_d/2$ and half-height h are considered. The first interesting conclusion is the fact that, in the two square ducts, the side-wall boundary layers extend up to almost the core of the duct, with a value of $\delta_{99,z} \simeq 0.84h$. If the aspect ratio is increased to 3 or 5, the side-wall boundary layer spans approximately the same percentage of the spanwise extent, around 70%, and the respective thicknesses increase from around $2.11h$ to $3.48h$ in these two cases. Moreover, for wider ducts the ratio between the side-wall boundary-layer thickness and the duct width progressively reduces from around 67% in AR = 7 to 38% in AR = 14.4, whereas the thickness remains approximately constant and equal to $\delta_{99,z} \simeq 5h$ in the three cases. It is interesting to note that this evolution shares several common features with the $\langle K \rangle_y$ distributions presented in Fig. 9, such as the different behavior of the square duct, where the insufficient width does not allow a complete development of the side-wall boundary layer. The AR = 3 and 5 cases, which showed an intermediate distribution in Fig. 9 with a developing but slightly constrained secondary flow, also exhibit an intermediate behavior here. Thus, these cases show developing boundary layers spanning a significant portion of the duct width. Moreover, higher aspect ratios lead to a maximum side-wall boundary-layer thickness of around $5h$, which is precisely the spanwise distance from the corner up to which the secondary flow exhibited noticeable energy

as shown in Fig. 9 (right). This is a remarkable conclusion, which indicates that there may be connections between the two three-dimensional effects present in turbulent rectangular ducts. With respect to Reynolds-number effects, they are only noticeable, although still low, in the AR = 3 at $\mathrm{Re}_{\tau,c} \simeq 360$ case which exhibits 8% increase in $\delta_{99,z}$ with respect to the $\mathrm{Re}_{\tau,c} \simeq 180$ one. This is probably connected with the higher K_{total} value reported in Table III for the AR = 3 case, whereas in the square duct the total energy of the secondary flow remained approximately invariant with Reynolds number.

V. TURBULENCE STATISTICS AND WALL-SHEAR STRESS DISTRIBUTIONS

In this section, we analyze turbulence statistics from the various duct cases and compare them with those exhibited by spanwise-periodic channel flows. Note that the results from Sec. IV show that the kinetic energy of the secondary flow K is very small for $z_c > 5h$, and therefore it is interesting to compare the center-plane statistics of the widest ducts, i.e., those with AR = 7, 10, and 14.4, with the ones of the periodic channels, where no secondary flow is present. In Fig. 11 (top), we show the inner-scaled mean flow and the Reynolds-stress tensor components from the three duct cases mentioned above and compare these profiles with the channel flow data reported in Ref. [42] at $\mathrm{Re}_\tau = 180$. The agreement of mean flow, fluctuations, and Reynolds-shear stress is excellent among ducts and also with the channel, and the maximum deviations, observed in the inner peak of the streamwise velocity fluctuations, are around 1%, which is the order of statistical accuracy of the data presented in this study. Moreover, in Fig. 11 (bottom) the turbulent kinetic energy (TKE) budgets from AR = 10 and 14.4 at $z/h \simeq 0$ are compared with the ones from the channel [42]. These profiles also reveal an excellent agreement between the two ducts and the channel (note that the AR = 7 case, not shown, is also in very good agreement with the channel). The time- and streamwise-averaged statistics at the core of duct with AR > 7 are essentially the same as those obtained from a spanwise-periodic channel. Nevertheless, since the core region, unaffected by secondary-flow effects, would be quite narrow in an AR = 7 configuration, an aspect ratio of at least 10 would be recommended in an experiment aiming at reproducing spanwise-periodic channels conditions at the center plane. The effect of side walls on the wall-shear stress in rectangular ducts up to aspect ratios of 10 and 50 was studied experimentally by Knight and Patel [43] and by Rhodes and Knight [44], respectively. In these studies, the ratio of $\overline{\tau}_w$ (wall-shear stress averaged over the perimeter) and the wall-shear stress obtained from the streamwise pressure gradient was determined. As discussed by Monty [45], this ratio would be one in the idealized case of infinite aspect ratio. After analyzing both sets of experiments, Rhodes and Knight [44] concluded that a minimum aspect ratio of 10 is required to minimize the impact of the side walls on the skin friction, a conclusion which is in good agreement with the results presented here.

In Fig. 12, we show wall-shear stress distributions from the various duct cases, including mean wall-shear stress, as well as streamwise and spanwsie root-mean-square (rms) profiles, as functions of the inner-scaled spanwise coordinate z_c^+ (where $u_{\tau,c}$ was used for the scaling). We will first focus on the aspect-ratio effects studied in Fig. 12 at $\mathrm{Re}_{\tau,c} \simeq 180$, and in particular on the mean wall-shear stress distributions. The square-duct case exhibits a maximum at $z_c^+ \simeq 50$, followed by a local minimum separated a spanwise distance of $\lambda_z^+/2 \simeq 50$, which forms a high- and low-speed streak pair [10,11]. Beyond this point, and approximately at $z_c^+ \simeq 180$, another local maximum is observed, which is located at the duct center plane. In the square-duct case, the inner-scaled half-width is $W_d^+/2 \simeq 180$, which means that one half of the inner-scaled spanwise extent of the duct allows us to allocate just three streaks (keeping in mind the distance of $\simeq 50^+$ between the corner and the first one). At higher aspect ratios, the location of the first maximum is approximately constant and equal to $z_c^+ \simeq 50$, which implies that the geometry (in this case the corner) determines the location of the first streak and that it is a high-speed streak. Moreover, the value of this first maximum decreases with AR, from around $\tau_w/\tau_{w,c} \simeq 1$ in the first duct to around 0.8 in aspect ratios beyond 7. All the aspect-ratio cases exhibit a local minimum at a distance of around $\lambda_z^+/2 \simeq 50$ from the maximum, forming the high- and low-speed streak pair, but beyond this point there is not a defined third streak in

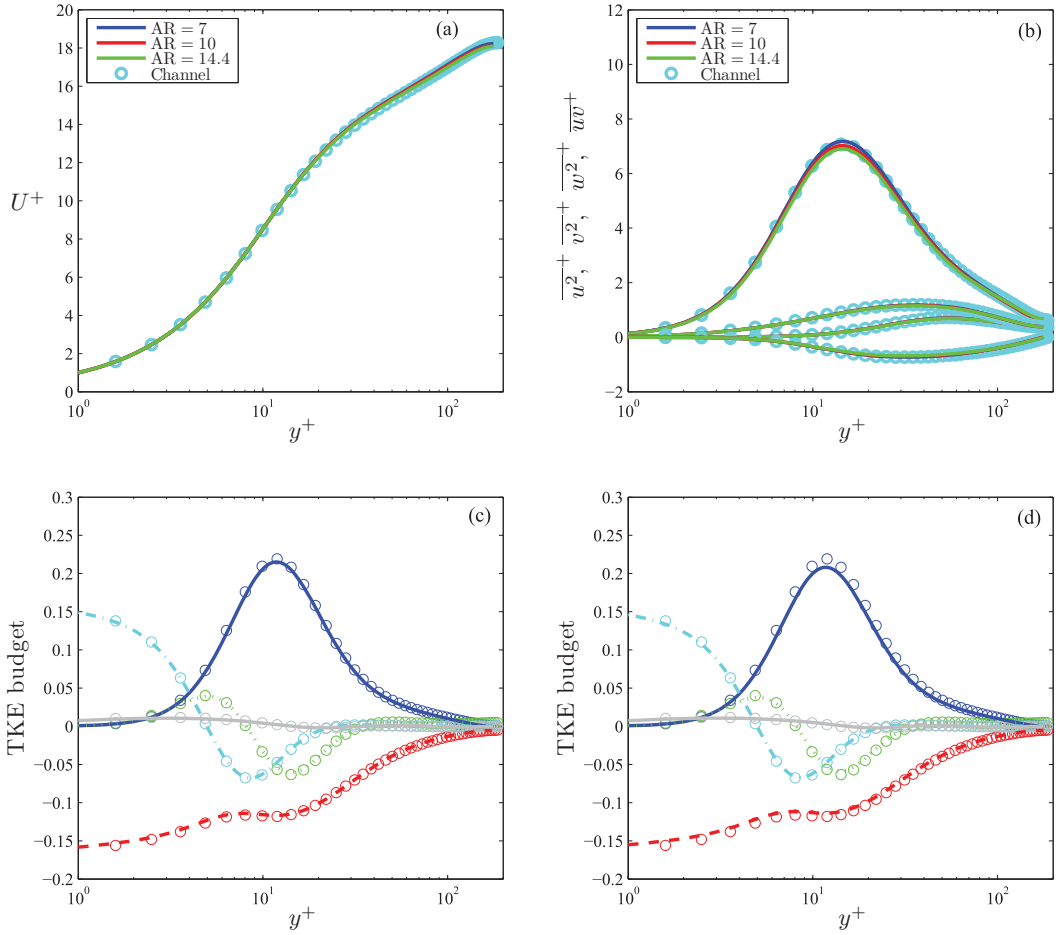

FIG. 11. (a) Inner-scaled mean flow and (b) Reynolds-stress tensor components at the center plane of various ducts with $\mathrm{Re}_{\tau,c} \simeq 180$, compared with DNS of channel flow at $\mathrm{Re}_\tau = 180$ [42]. TKE budget of ducts at $\mathrm{Re}_{\tau,c} \simeq 180$ with (c) AR = 10 and (d) AR = 14.4, compared with same reference channel flow data [42]. TKE budget terms: ——— production, - - - - dissipation, ... turbulent transport, -·-·-·- viscous diffusion, and ——— velocity-pressure-gradient correlation.

the cases with AR $\geqslant$ 3. Pinelli *et al.* [9] observed a similar behavior at progressively higher Re, which also leads to larger inner-scaled duct widths, and the idea is that larger values of W_d^+ allow allocation of higher numbers of streaks. This produces a behavior closer to that exhibited by spanwise-periodic channels at the core of the duct. This is also consistent with the recent work by Spalart *et al.* [25], who showed that for asymptotic Re the wall-shear stress distribution in turbulent ducts would tend toward a uniform value (except close to the corners). In their study, they used matching arguments of the inner and outer regions, leading to a logarithmic overlap layer in the mean velocity profile. Whereas the higher maximum observed in the square case is explained by the constraining effect of the width, for AR $\geqslant$ 7 the behavior close to the corner remains unchanged. Beyond the high- and low-speed streak pair, the wall-shear stress curves rise toward the center-plane value, and interestingly the cases with AR $\geqslant$ 7 exhibit a region of approximately constant $\tau_w/\tau_{w,c} \simeq 1$ beyond $z_c/h \simeq 5$, which as discussed in Sec. IV is the region where the secondary flow becomes significantly attenuated.

Another interesting quantity analyzed in Fig. 12 for all the cases at $\mathrm{Re}_{\tau,c} \simeq 180$ is the rms of the wall-shear stress, both in the streamwise and the spanwise directions, which shows the influence of

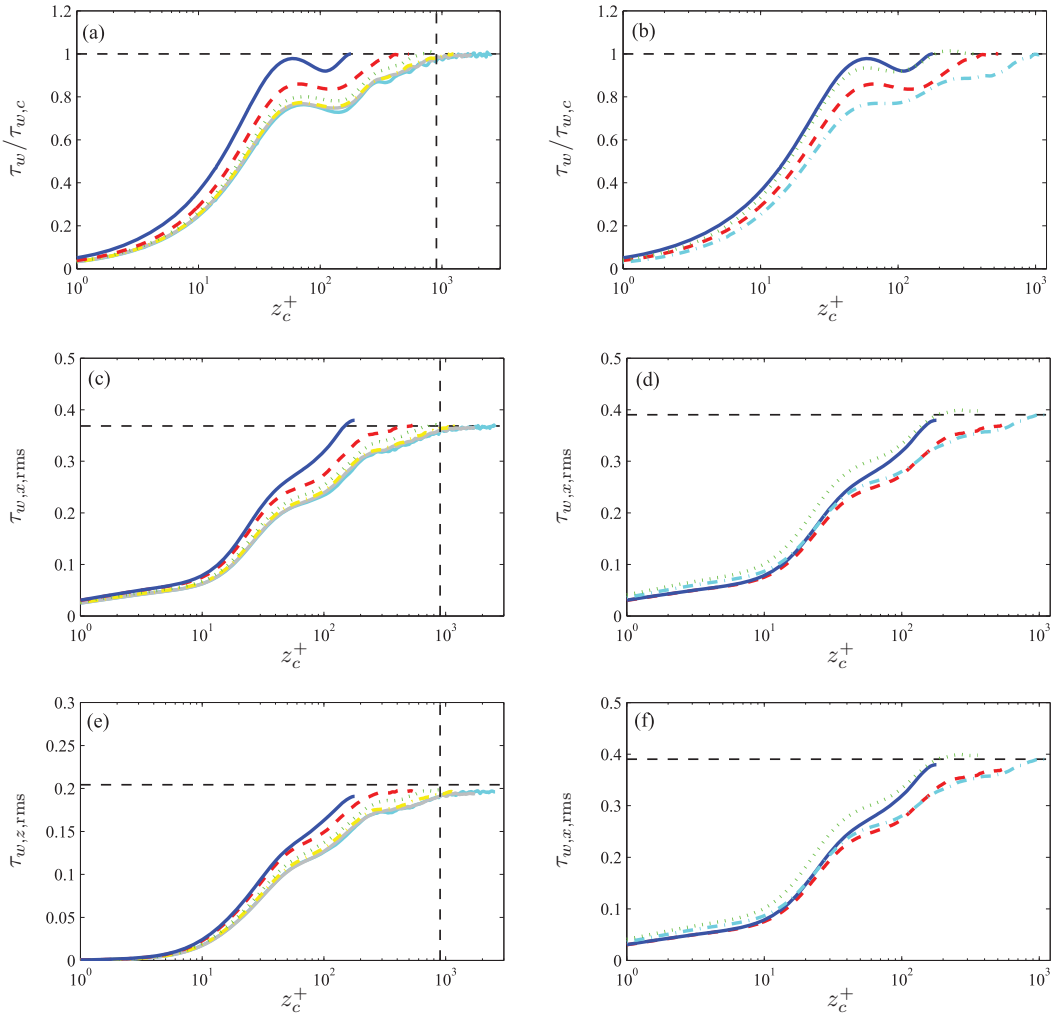

FIG. 12. Spanwise distributions of [(a), (b)] wall-shear stress normalized with center-plane value and [(c), (d)] streamwise and [(e), (f)] spanwise fluctuating wall-shear stress. The variable z_c^+ is defined with its origin at the corner and is formed with $u_{\tau,c}$. The cases shown in the left panels correspond to ——— AR = 1, - - - - AR = 3, ····· AR = 5, ——— AR = 7, ——— AR = 10, and ——— AR = 14.4, all of them at $\mathrm{Re}_{\tau,c} \simeq 180$, and the vertical – – – – indicates the position where $z_c = 5h$. The cases shown in the right panels are ——— AR = 1 and - - - - AR = 3 at $\mathrm{Re}_{\tau,c} \simeq 180$ and ····· AR = 1 and - · - · AR = 3 at $\mathrm{Re}_{\tau,c} \simeq 360$. In all the panels, the horizontal – – – – represents corresponding channel flow values at the same Re_τ [42,47].

the large-scale motions on the outer region with the the structures near the wall [46]. As in the mean wall-shear stress, the behavior observed in the square duct differs slightly from that of the wider ones, also due to the limited spanwise width. All the cases show an inflection in $\tau_{w,x,\mathrm{rms}}$ and $\tau_{w,z,\mathrm{rms}}$, at the same location where the the mean wall shear has the first maximum, i.e., $z_c^+ \simeq 50$. This is connected with the interactions between the outer-layer structures and the near wall, and it is also important to note that a second (more subtle, especially in the case of the spanwise-fluctuating shear stress) inflection point is observed at $z_c^+ \simeq 100$. This is the spanwise position where the low-speed streak is located. Toward the center plane, the square duct reaches values slightly different from those of the spanwise-periodic channel [42] at $\mathrm{Re}_\tau = 180$, although the cases with AR $\geqslant 3$ essentially

converge toward the channel flow values at $z/h \simeq 0$. Thus, and as it is the case in channel flows, the streamwise-fluctuating wall-shear stress is higher than the spanwise component because of the elongated nature of the large-scale motions in the outer flow, which essentially modulate the near-wall fluctuations. As in the case of the mean wall-shear stress, the widest ducts with AR $\geqslant 7$ exhibit a plateau in the two fluctuating components beyond $z_c/h \simeq 5$, reaching the same values as those in the spanwise-periodic channel.

Reynolds-number effects on the wall-shear stress distributions are also assessed in Fig. 12, where the spanwise evolutions of the mean and fluctuating stresses are shown for the AR = 1 and 3 cases at $\mathrm{Re}_{\tau,c} \simeq 180$ and 360. The latter are compared with the values from the spanwise-periodic channel by Lenaers *et al.* [47]. The higher Re cases also exhibit a maximum at $z_c^+ \simeq 50$ and a local minimum at $z_c^+ \simeq 100$, which as discussed above constitutes a high- and low-speed streak pair, and the position of the high-speed streak is determined by the corner. The square duct at $\mathrm{Re}_{\tau,c} \simeq 360$ shows another relative maximum at $z_c^+ \simeq 180$, similar to the lower Re case, and beyond this point it smoothly converges toward the center-plane value. Note that in this case the inner-scaled half-width is $W_d^+/2 \simeq 360$, which in principle would allow us to allocate around seven streaks. Although the positions of the three first ones are essentially determined by the geometry, the remaining four toward the core of the duct start to exhibit features characteristic of the channel flow, in the sense that there is not a preferential location for the streaks, and as also pointed out in Ref. [9] this leads to the progressively more uniform wall-shear stress trend. In the case of the AR = 3 duct at $\mathrm{Re}_{\tau,c} \simeq 180$, the wider $W_d^+/2 \simeq 540$ leads to at least 10 streaks, and only the first high- and low-speed streak pair is determined by the corner. Beyond this point, the curve evolves toward the center-plane value, without clearly exhibiting the second maximum at $z_c^+ \simeq 180$. Similarly, the higher Re case with aspect ratio of 3 also shows the first streak pair, but beyond this point there is not a clear signature of the geometry on this curve. Regarding the fluctuating components, the higher Reynolds number cases also show inflection points at $z_c^+ \simeq 50$ and 100, locations at which the high- and low-speed streaks are located, and interestingly at $\mathrm{Re}_{\tau,c} \simeq 360$ the two ducts converge toward the fluctuating wall-shear stress values reported by Lenaers *et al.* [47] for spanwise-periodic channel flows. It is interesting to note that in the streamwise-fluctuating wall-shear stress the effect of Reynolds number is moderate in the square duct and subtle in the AR = 3 case. In fact, in the aspect ratio 3 duct the $\tau_{w,x,\mathrm{rms}}$ curve at $\mathrm{Re}_{\tau,c} \simeq 360$ is only above the one at 180 when z_c exhibits the inner-scaled half-width of the lower Reynolds number duct $W_d^+/2 \simeq 540$. Below this point, the two curves are very similar. On the other hand, the $\tau_{w,z,\mathrm{rms}}$ curves from the two $\mathrm{Re}_{\tau,c} \simeq 360$ cases are above the ones of the 180 ducts throughout the whole spanwise direction. This is consistent with the fact that the increase of $\tau_{w,x,\mathrm{rms}}$ in channel flows is significantly below the increase in $\tau_{w,z,\mathrm{rms}}$ when increasing Re_τ from 180 to 360 (8.33% compared with 20%). A trend similar to the one from channel flows was reported in Ref. [32] for pipe flows and in Ref. [48] for zero-pressure-gradient turbulent boundary layers in this Reynolds-number range, although in those cases the trends of $\tau_{w,x,\mathrm{rms}}$ and $\tau_{w,z,\mathrm{rms}}$ started to level off beyond $\mathrm{Re}_\tau \simeq 1{,}000$, a Reynolds number at which the streamwise component is around 40% higher than the spanwise one.

VI. SUMMARY AND CONCLUSIONS

Direct numerical simulations of turbulent duct flows with aspect ratios 1, 3, 5, 7, 10, and 14.4 at a friction Reynolds number $\mathrm{Re}_{\tau,c} \simeq 180$, and aspect ratios 1 and 3 at $\mathrm{Re}_{\tau,c} \simeq 360$, were carried out with the spectral-element code NEK5000. The aim of these simulations was to gain insight into the characteristics of Prandtl's secondary flow of second kind, its evolution with aspect ratio and Reynolds number, and its impact on the flow physics of wall-bounded turbulence. The computational setup was adequate to capture the smallest turbulent structures, as well as the complicated phenomena arising at the duct corners. Although the corners inhibit the formation of typical wall-turbulence streaks, the interaction of bursting mechanisms from horizontal and vertical walls lead to the formation of the secondary flow through redistribution of turbulent kinetic energy from the $\overline{v^2}$ component to the $\overline{w^2}$.

The secondary flow in the various ducts is first characterized from a topological point of view by means of the stream function of the mean cross flow. We find that, for the square duct, increasing Reynolds number leads to a secondary flow pattern stretched toward the duct core, with the vortex centers moving away from the walls. This, as was also observed by Pinelli *et al.* [9], highlights the multiscale character of the secondary flow of Prandtl's second kind. For $\mathrm{Re}_{\tau,c} \simeq 180$, increasing the aspect ratio leads to the progressively spanwise development of the vortex on the horizontal wall, which extends up to $z_c/h \simeq 4$ in the widest ducts with aspect ratios larger or equal to 7. For these wider ducts, the position of the center of this secondary vortex remains approximately constant with aspect ratio. Concurrently, the vortex on the vertical wall becomes significantly compressed horizontally due to the substantial development of the vortex along the horizontal wall, and its center also remains approximately at the same position with increasing AR. Regarding Re effects in the AR $= 3$ case, although the vortex on the vertical wall becomes more elongated at higher Re, its center does not significantly change location. The vortex along the horizontal wall becomes more stretched toward the corner, its center moves farther away from the wall, and it produces more acceleration of the flow moving parallel to the horizontal wall.

The magnitude of the secondary flow is quantified in terms of the cross-plane mean kinetic energy $K = 1/2(V^2 + W^2)$, and its variation in the spanwise direction is assessed in the various cases. Our results show that averaging times of at least 3000 convective time units are required to reach a converged state of the secondary flow, which extends up to $z_c/h \simeq 5$ in sufficiently wide ducts, i.e., AR > 5. We also show that if the duct is not wide enough to accommodate the whole extent of the secondary flow, then its structure is modified, resulting in a different spanwise distribution of energy. Our results also indicate that long-time averages of statistics in a region of sufficient width around the vertical center plane of rectangular ducts with aspect ratios larger than 10 are in close agreement with the ones obtained in spanwise-periodic channels. Thus, aspect ratios of at least 10 are required in experimental facilities to obtain such conditions in the core of the duct. The facility used by Zanoun *et al.* [49] benefited in its design from the many earlier studies concluding that an aspect ratio of 12 was sufficient to emulate a canonical channel flow. Larger values have been suggested by some more recent experimental studies, such as those by Vinuesa *et al.* [29], and in much earlier references not generally cited in recent literature but discussed in Ref. [28]. In the study of Vinuesa *et al.* [29], certain aspects such as the tripping, uncertainties in the position of the Pitot tube, and the Reynolds-number range, may have contributed to the larger aspect ratios recommended to ensure two-dimensionality of the core flow. Furthermore, from the current results, with the approach of dividing the flow into windows of width h, we reach a number of interesting conclusions: First, all the rectangular ducts exhibit similar levels of averaged energy close to the corner (window 1), $\langle K \rangle_{yz1} \simeq 4.5\times10^{-5}$ and 4×10^{-5} for aspect ratios 3 and 5, and 7, 10, and 14.4, respectively; the square duct shows a lower level $\simeq 3\times10^{-5}$; and its secondary flow differs from the one observed in the wider ducts. In addition, the second window shows the same level of energy in all aspect ratios from 3 to 14.4, $\langle K \rangle_{yz2} \simeq 2\times10^{-5}$, which is roughly four times larger than the energy found in the third window for the widest cases (7, 10, and 14.4). Interestingly, all the windows beyond no. 5 exhibit a decaying level of energy, and the rate of decay is approximately $\langle K \rangle_{yz} \sim t_a^{-1}$. This is the same rate of decay observed in a spanwise-periodic simulation, which suggests that beyond $z_c/h \simeq 5$, $\langle K \rangle_{yz}$ behaves as a random variable with zero mean, with rate of decay consistent with central limit theorem. With respect to windows 4 and 5, the levels of energy from the various cases do not decay at the rate $\langle K \rangle_{yz} \sim t_a^{-1}$. It can be stated that the flow in this region does not behave as it does in spanwise-periodic channels.

In closing, based on all the above results, we conclude that since long-time averages of statistics in the core region of rectangular ducts, spanning about the width of a well-designed channel simulation (i.e., extending about $\simeq 3h$ on each side of the center plane), are similar to results from computations of the canonical channel flow, one may utilize ducts or experimental facilities with aspect ratios larger than 10 to compare their time-averaged information with results obtained from spanwise-periodic channel simulations.

ACKNOWLEDGMENTS

The simulations were performed on resources provided by the Swedish National Infrastructure for Computing (SNIC) at the Center for Parallel Computers (PDC), in KTH, Stockholm, and by the Argonne Leadership Computing Facility (ALCF) at the Argonne National Laboratory (ANL), which is supported by the Office of Science of the US Department of Energy. R.V. and P.S. acknowledge the funding provided by the Knut and Alice Wallenberg Foundation and the Swedish Research Council (V.R.).

[1] R. Vinuesa, A. Noorani, A. Lozano-Durán, G. K. El Khoury, P. Schlatter, P. F. Fischer, and H. M. Nagib, Aspect ratio effects in turbulent duct flows studied through direct numerical simulation, J. Turbul. **15**, 677 (2014).

[2] L. Prandtl, Über die ausgebildete Turbulenz [Turbulent Flow], Verh. Second Intl Kong. NACA Tech. Memo 62, Second Intl Kong. für Tech. Mech., Zürich (1926), p. 435.

[3] P. R. Spalart, Strategies for turbulence modelling and simulations, Int. J. Heat Fluid Flow **21**, 252 (2000).

[4] A. Huser and S. Biringen, Direct numerical simulation of turbulent flow in a square duct, J. Fluid Mech. **257**, 65 (1993).

[5] L. C. Hoagland, Fully developed turbulent flow in straight rectangular ducts: Secondary flow, its cause and effect on the primary flow, Ph.D. thesis, Massachusetts Institute of Technology, Cambridge, MA, 1962 (unpublished).

[6] F. B. Gessner and J. B. Jones, On some aspects of fully-developed turbulent flow in rectangular channels, J. Fluid Mech. **23**, 689 (1965).

[7] F. B. Gessner, The origin of secondary flow in turbulent flow along a corner, J. Fluid Mech. **58**, 1 (1973).

[8] S. Gavrilakis, Numerical simulation of low-Reynolds-number turbulent flow through a straight square duct, J. Fluid Mech. **244**, 101 (1992).

[9] A. Pinelli, M. Uhlmann, A. Sekimoto, and G. Kawahara, Reynolds number dependence of mean flow structure in square duct turbulence, J. Fluid Mech. **644**, 107 (2010).

[10] S. J. Kline, W. C. Reynolds, F. A. Schraub, and P. W. Runstadler, The structure of turbulent boundary layers, J. Fluid Mech. **30**, 741 (1967).

[11] A. K. Gupta, J. Laufer, and R. E. Kaplan, Spatial structure in the viscous sublayer, J. Fluid Mech. **50**, 493 (1971).

[12] O. Marin, R. Vinuesa, A. V. Obabko, and P. Schlatter, Characterization of the secondary flow in hexagonal ducts, Phys. Fluids **28**, 125101 (2016).

[13] M. Uhlmann, A. Pinelli, G. Kawahara, and A. Sekimoto, Marginally turbulent flow in a square duct, J. Fluid Mech. **588**, 153 (2007).

[14] B. R. Owolabi, R. J. Poole, and D. J. C. Dennis, Experiments on low-Reynolds-number turbulent flow through a square duct, J. Fluid Mech. **798**, 398 (2016).

[15] A. Samanta, R. Vinuesa, I. Lashgari, P. Schlatter, and L. Brandt, Enhanced secondary motion of the turbulent flow through a porous square duct, J. Fluid Mech. **784**, 681 (2015).

[16] Z.-J. Zhu, H.-X. Yang, and T.-Y. Chen, Direct numerical simulation of turbulent flow in a straight square duct at Reynolds number 600, J. Hydrodynam. **21**, 600 (2009).

[17] H. Raisei, U. Piomelli, and A. Pollard, Evaluation of turbulence models using direct numerical simulation and large-eddy simulation data, J. Fluids Eng. **133**, 1 (2011).

[18] H. Zhang, F. X. Trias, A. Gorobets, Y. Tan, and A. Oliva, Direct numerical simulation of a fully developed turbulent square duct flow up to $Re_\tau = 1200$, Int. J. Heat Fluid Flow **54**, 258 (2015).

[19] S. Pirozzoli, D. Modesti, P. Orlandi, and F. Grasso, Turbulence and secondary motions in square duct flow, J. Fluid Mech. **840**, 631 (2018).

[20] D. Krasnov, O. Zikanov, and T. Boeck, Numerical study of magnetohydrodynamic duct flow at high Reynolds and Hartmann numbers, J. Fluid Mech. **704**, 421 (2012).

[21] R. Vinuesa, C. Prus, P. Schlatter, and H. M. Nagib, Convergence of numerical simulations of turbulent wall-bounded flows and mean cross-flow structure of rectangular ducts, Meccanica **51**, 3025 (2016).
[22] R. K. Madabhushi and S. P. Vanka, Large eddy simulation of turbulence-driven secondary flow in a square duct, Phys. Fluids **3**, 2734 (1991).
[23] M. Breuer and W. Rodi, Large-eddy simulation of turbulent flow through a straight square duct and a 180° bend, in *Direct and Large-Eddy Simulation I*, edited by P. R. Voke, L. Kleiser, and J.-P. Chollet (Springer, Netherlands, 1994), pp. 273–285.
[24] J. Yao, Y. L. Zhao, and M. Fairweather, Numerical simulation of turbulent flow through a straight square duct, Appl. Therm. Eng. **91**, 800 (2015).
[25] P. R. Spalart, A. Garbaruk, and A. Stabnikov, On the skin friction due to turbulence in ducts of various shapes, J. Fluid Mech. **838**, 369 (2018).
[26] J. Ohlsson, P. Schlatter, P. F. Fischer, and D. S. Henningson, Direct numerical simulation of separated flow in a three-dimensional diffuser, J. Fluid Mech. **650**, 307 (2010).
[27] H. S. Choi and T. S. Park, The influence of streamwise vortices on turbulent heat transfer in rectangular ducts with various aspect ratios, Int. J. Heat Fluid Flow **40**, 1 (2013).
[28] R. Vinuesa, P. Schlatter, and H. M. Nagib, On minimum aspect ratio for duct flow facilities and the role of side walls in generating secondary flows, J. Turbul. **16**, 588 (2015).
[29] R. Vinuesa, E. Bartrons, D. Chiu, K. M. Dressler, J.-D. Rüedi, Y. Suzuki, and H. M. Nagib, New insight into flow development and two dimensionality of turbulent channel flows, Exp. Fluids **55**, 1759 (2014).
[30] P. F. Fischer, J. W. Lottes, and S. G. Kerkemeier, NEK5000: Open source spectral element CFD solver, http://nek5000.mcs.anl.gov.
[31] A. T. Patera, A spectral element method for fluid dynamics: Laminar flow in a channel expansion, J. Comput. Phys. **54**, 468 (1984).
[32] G. K. El Khoury, P. Schlatter, A. Noorani, P. F. Fischer, G. Brethouwer, and A. V. Johansson, Direct numerical simulation of turbulent pipe flow at moderately high Reynolds numbers, Flow Turbul. Combust. **91**, 475 (2013).
[33] R. Vinuesa, L. Fick, P. Negi, O. Marin, E. Merzari, and P. Schlatter, Turbulence statistics in a spectral-element code: A toolbox for high-fidelity simulations, Tech. Rep. ANL/MCS-TM-367, 2017 Argonne National Lab. (ANL), Argonne, IL (United States).
[34] C. Chin, A. S. H. Ooi, I. Marusic, and H. M. Blackburn, The influence of pipe length on turbulence statistics computed from direct numerical simulation data, Phys. Fluids **22**, 115107 (2010).
[35] J. Klewicki, C. Chin, H. M. Blackburn, A. Ooi, and I. Marusic, Emergence of the four layer dynamical regime in turbulent pipe flow, Phys. Fluids **24**, 045107 (2012).
[36] R. L. Panton, in *Incompressible Flow*, 2nd ed. (Wiley-Interscience, Hoboken, NJ, 1996), pp. 213–216.
[37] P. Schlatter and R. Örlü, Turbulent boundary layers at moderate Reynolds numbers: Inflow length and tripping effects, J. Fluid Mech. **710**, 5 (2012).
[38] S. Hoyas and J. Jiménez, Reynolds number effects on the Reynolds-stress budgets in turbulent channels, Phys. Fluids **20**, 101511 (2008).
[39] A. Lozano-Durán and J. Jiménez, Effect of the computational domain on direct simulations of turbulent channels up to $\mathrm{Re}_\tau = 4200$, Phys. Fluids **26**, 011702 (2014).
[40] M. Lee and R. D. Moser, Direct numerical simulation of turbulent channel flow up to $\mathrm{Re}_\tau \simeq 5200$, J. Fluid Mech. **774**, 395 (2015).
[41] M. Chevalier, P. Schlatter, A. Lundbladh, and D. S. Henningson, A pseudospectral solver for incompressible boundary layer, Technical Report TRITA-MEK 2007:07, KTH Mechanics, 2007 (unpublished).
[42] J. C. del Álamo and J. Jiménez, Spectra of the very large anisotropic scales in turbulent channels, Phys. Fluids **15**, 41 (2003).
[43] D. W. Knight and H. S. Patel, Boundary shear in smooth rectangular ducts, J. Hydraul. Eng. **111**, 29 (1985).
[44] D. G. Rhodes and D. W. Knight, Distribution of shear force on boundary of smooth rectangular duct, J. Hydraul. Eng. **120**, 787 (1994).
[45] J. P. Monty, Developments in smooth wall turbulent duct flows, Ph.D. thesis, University of Melbourne, Australia, 2005 (unpublished).

[46] R. Örlü and P. Schlatter, On the fluctuating wall-shear stress in zero pressure-gradient turbulent boundary layer flows, Phys. Fluids **23**, 021704 (2011).

[47] P. Lenaers, Q. Li, G. Brethouwer, P. Schlatter, and R. Örlü, Rare backflow and extreme wall-normal velocity fluctuations in near-wall turbulence, Phys. Fluids **24**, 035110 (2012).

[48] P. Schlatter and R. Örlü, Assessment of direct numerical simulation data of turbulent boundary layers, J. Fluid Mech. **659**, 116 (2010).

[49] E.-S. Zanoun, F. Durst, and H. M. Nagib, Evaluating the law of the wall in two-dimensional fully developed turbulent channel flows, Phys. Fluids **15**, 3079 (2003).